Accepted Manuscript

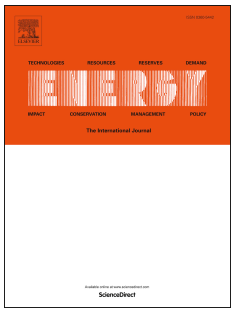

A novel upscaling procedure for characterising heterogeneous shale porosity from nanometer-to millimetre-scale in 3D

Lin Ma, Patrick J. Dowey, Ernest Rutter, Kevin G. Taylor, Peter D. Lee

PII: S0360-5442(19)31135-1

DOI: https://doi.org/10.1016/j.energy.2019.06.011

Reference: EGY 15494

To appear in: *Energy*

Received Date: 15 October 2018

Revised Date: 29 May 2019

Accepted Date: 2 June 2019

Please cite this article as: Ma L, Dowey PJ, Rutter E, Taylor KG, Lee PD, A novel upscaling procedure for characterising heterogeneous shale porosity from nanometer-to millimetre-scale in 3D, *Energy* (2019), doi: https://doi.org/10.1016/j.energy.2019.06.011.

A novel upscaling procedure for characterising heterogeneous shale porosity from nanometre- to millimetre-scale in 3D

Ma, Lin[1*], Dowey, Patrick J. [1], Rutter, Ernest[1], Taylor, Kevin G.[1], Lee, Peter D.[2, 3],

[1] School of Earth and Environmental Sciences, The University of Manchester, Manchester, M13 9WJ, UK

[2] Research Complex at Harwell, RAL, Didcot, OX11 0FA

[3] UCL Mechanical Engineering, Torrington Place, London, WC1E 7JE

* Corresponding author: lin.ma@manchester.ac.uk

Abstract

Microstructures and pore systems in shales are key to understanding the role of shale in many energy applications. This study proposes a novel multi-stage upscaling procedure to comprehensively investigate the heterogeneous and complex microstructures and pore systems in a laminated and microfractured shale, utilizing 3D multi-scale imaging data. Five imaging techniques were used for characterisation from sub-nanoscale to macroscale (core-scale), spanning four orders of magnitude. Image data collected using X-ray tomography, Focused Ion Beam, and Electron Tomography techniques range in voxel size from 0.6 nm to 13 µm.

Prior to upscaling, a novel two-step analysis was performed to ensure sub-samples were representative. Following this, a three-step procedure, based on homogenising descriptors and computed volume coefficients, was used to upscale the quantified microstructure and pore system. At the highest resolution (nanoscale), four distinct pore types were identified. At the sub-micron scale equations were derived for three pore-associated phases. At the microscale, the volume coefficients were recalculated to upscale the pore system to the macroscale (millimetre). The accuracy of the upscaling methodology was verified, predicting the total porosity within 7.2 % discrepancy. The results provide a unique perspective to understand

heterogeneous rock types, breaking though prior scale limitations in the pore system.

Keywords

Multi-scale; pore system; upscaling; shale; X-ray tomography; FIB-SEM;

Highlights:

- A novel upscaling method is proposed to quantify pores from the nm- to mm-scale.
- Three advanced 3D imaging techniques are applied across five distinct scales.
- A two-step analysis prior to upscaling ensures the images are representative.
- Four types of pores are recognized at nanoscale and then all upscaled to mm-scale.
- Upscaled porosity differs by less than 10% compared to measured helium porosity.

1 Introduction

Shales (fissile mudstones) contribute greatly to many energy applications but are still arguably one of the least understood rock types (Schieber et al., 1998). Shales are targets for global hydrocarbon exploration (Jarvie, 2012), potential reservoirs and cap rocks for gas (Aplin and Macquaker, 2011) and carbon storage (Busch et al., 2008) and repositories for nuclear waste disposal (Joyce et al., 2014). However, the environmentally-safe exploitation of shales requires an improved understanding of their complex microstructure and pore systems。

Shale microstructure and pore systems have been the subject of numerous academic studies over the last decade. However, due to their strong heterogeneity from the nanometer to basin scales shales remain relatively poorly understood. This has been recognized in many shale formations including the Barnett Shale (Loucks et al., 2009), Woodford Shale (Slatt and O'Brien, 2011), Marcellus Shale (Klaver et al., 2015) and Haynesville-Bossier Shale (Milliken et al., 2013). Shale microstructure and pores can be imaged at a resolution from a few to hundreds of nanometers with high-resolution SEM imaging techniques such as broad ion beam-scanning electron microscopy (BIB-SEM) in 2D (Klaver et al., 2015) and focused

ion beam-scanning electron microscopy (FIB-SEM) in 3D at nm-scale (Curtis et al., 2010). The distribution of shale components such as organic matter (Ma et al., 2017b), large mineral grains (Keller et al., 2013) and clay minerals (Ma et al., 2016) can be imaged in 3D with X-ray computed tomography (XCT) from mm-scale to μm-scale. Due to the highly heterogeneous nature of shales and the limitations of current imaging techniques, all relevant features cannot be resolved at a single scale (Ma et al., 2017a). Therefore, imaging across multiple scales, and integration between different scales, is essential accurately to characterize shale properties.

A few recent studies have performed upscaling across two or more scales, but these approaches were frequently limited to bridging only a single order of magnitude in scale (Zhang et al., 2012), or in bridging directly from the nano- to macroscale (Peng et al., 2015). Also, averaging (Kazemi et al., 2012) or geometrical methods (Chen et al., 2013) to describe porosity or kerogen, have provided a basis for upscaling. Using a single equation to bridge many scales ignores intermediate-scale heterogeneity, which limits its application. This study aims to build a multi-stage process to upscale the pores from nano-scale to macro-scale more precisely. This procedure relies on detailed study of the relationships between pore systems and related features. It employs five imaging techniques to quantify the microstructure and pore system in a typical shale sample. Fractures, sedimentary laminae, minerals, organic matter and pores are all comprehensively characterised at appropriate scales.

A novel two-step representative analysis was performed in the downscale sampling process from macroscale to sub-nanoscale and a three-step upscaling procedure was then performed from sub-nanoscale back to macroscale. This dual-representative analytical test ensures that the multiscale characterisation and quantification of microstructures and the pore system are representative. This is the first study to investigate a 3D microstructure and pore system across four orders of magnitude (10^{-9} to 10^{-4} m), utilising images at five imaging resolutions. This proposed upscaling method not only fully characterises the pore system, but also its relationship to other microstructural features in shales. This quantification can have important

implications for shale gas extraction and carbon sequestration, but the proposed multi-scale characterisation method potentially has wider applications in the energy and environmental fields, for example nuclear waste disposal (Joyce et al., 2014), geothermal reservoirs (Lichtner and Karra, 2014) and fuel cells (Lu et al., 2017).

2 Materials and Methods

A shale sample was selected at 3573 m depth from a borehole core in the Haynesville-Bossier Shale (the same as used in Ma et al., 2018). A standard thin section (30 μm thick) was mechanically polished for petrological, mineralogical and microstructural analysis, and a 1 mm^2 subarea of the sample was milled using an argon ion beam (PIP II, Gatan, Pleasanton, United States) for pore observation.

Bulk mineralogy was determined using X-ray Diffraction (XRD) with Topas software version 4.2. Total Organic Carbon (TOC) was measured using a carbon analyser at the University of Newcastle, U.K. (Leco, Michigan, United States). Bulk porosity was measured on 20 mm diameter cylinders using a helium (He) porosimeter (ResLab, Gent, Belgium) while pore-size distributions were measured by nitrogen (N_2) sorption using a surface area analyzer (ASAP 2010, Micromeritics, Norcross, United States). The N_2 data was analyzed using the Brunauer-Emmett-Teller (BET) theory (Brunauer et al., 1938) and pore volume and sizes were calculated using the Barrett-Joyner-Halenda (BJH) method (Barrett et al., 1951) on a dried sample.

The sample is organic-rich (TOC 3.70 ± 0.02 wt%), phyllosilicate-bearing (41%) and gas-mature (Ro 2.3%), which is considered typical of this shale formation (Wang et al., 2013). The helium porosity is 7.0 % ±0.1% at ambient pressure and the permeability measured by the pore pressure oscillation method (McKernan et al., 2017) ranges from 1.0×10^{-17} to 3.7×10^{-21} m^2 at a constant pore pressure of 23 MPa when the effective pressure is increased from 0 MPa to 70 MPa (Ma et al., 2018).

2.1 Multi-scale 3D image acquisition and analysis

Five techniques were used in this study to characterize features with length scale from 10^{-3} m to 10^{-9} m: that is macroscale (10^{-3} to 10^{-5} m), microscale (10^{-5} to 10^{-6} m), sub-micron scale (10^{-6} to 10^{-7} m), nanoscale (10^{-7} to 10^{-9} m), and sub-nanoscale (below 10^{-9} m). The data presented here were acquired from X-ray computed tomography (XCT) at macroscale, microscale, sub-micron scale, from Focused Ion Beam Scanning Electron Microscopy (FIB-SEM) at nanoscale, and Electron Tomography (ET) at sub-nanoscale (Figure 1). Macroscale and sub-micron scale XCT data were collected at the Manchester X-ray Imaging Facility (MXIF); microscale XCT at I13-2 Beamline at the Diamond Light Source (DLS) synchrotron (Beamtime MT4022); FIB-SEM at the Electron Microscopy (EM) Centre; and TEM at Photon Science Institute (PSI), the University of Manchester.

2.1.1 3D X-ray computed tomography (XCT)

A 15 mm^3 cubic sample, a 1 mm^3 and two 65 μm^3 samples were imaged at macroscale to sub-microscale (Figure 1) in a Nikon XT225 Custom Bay instrument, UK Diamond synchrotron and ZEISS UltraNano XCT (e.g. Ma et al., 2017b).

2.1.2 3D Focused Ion Beam Scanning Electron Microscope (FIB-SEM)

Two sites of FIB-SEM datasets with ~8 × 8 × 6 μm^3 were acquired using Nova NanoLab 600i (FEI, Hillsboro, United States) at nanoscale (Figure 1) (Ma et al., 2017b). The images were acquired by secondary electron detector with resolutions of around 10 nm in the *XY* plane and with a vertical slice spacing of 20 nm along the *Z* axis.

2.1.3 Electron tomography (ET)

Two sites (organic-rich and mineral-rich) in each sample (~600 nm length and width, 60 nm thick) were imaged at sub-nanoscale by Electron tomography (ET) using a scanning

transmission electron microscope (STEM) beam in an FEI Talos TEM (see Ma et al., 2018)

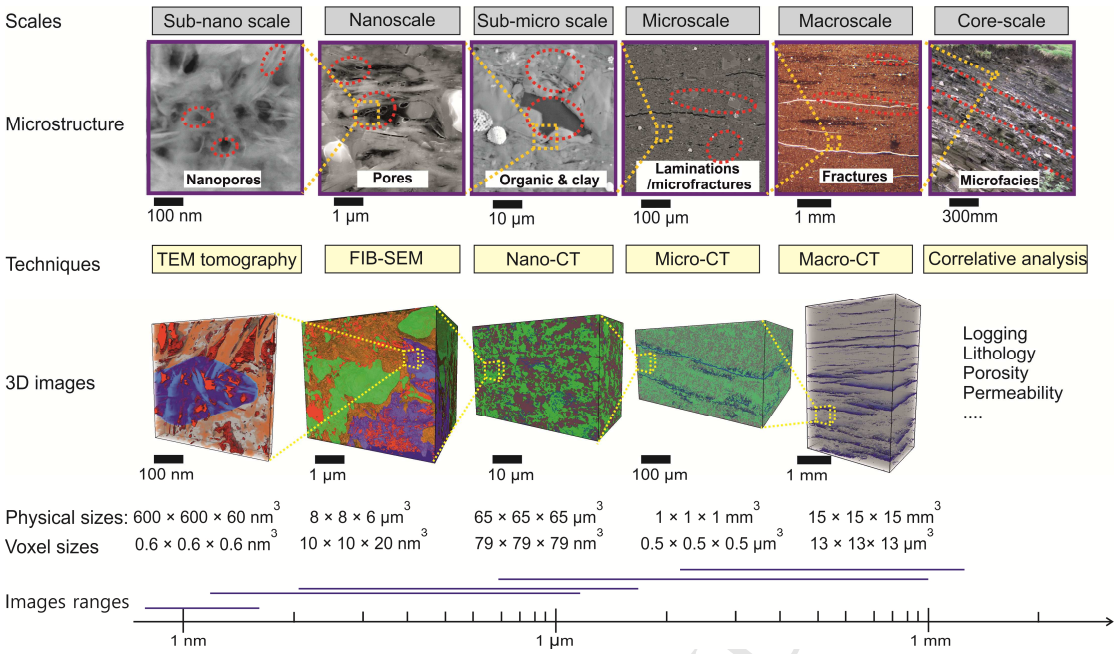

Figure 1 Multi-scale image acquisition using five specific imaging techniques (yellow dash box showing the similar volume sizes but not exact volumes selected from upper scale). The front plane is the *XY* plane and bedding (visible at the largest scale) is nominally parallel to the *XZ* plane. Red-pores, Brown- clay minerals, Blue- organic matter, pores and fractures, Green- granular minerals,

2.1.4 Image processing and quantification

Minor drift during the collection of FIB-SEM image slices required the additional application of alignment (rotation) and shearing corrections. Each XCT, FIB-SEM or TEM image dataset was then processed using a standard workflow with varied filtering, segmentation, and quantification methods (see Figure S2 in supplementary online materials for more details of image processing). Features below 27 voxels (3 × 3 × 3 for XYZ) for XCT data and 9 voxels (3 × 3 for XY plane) for FIB data were removed. The size, thickness, volume and surface area of each feature were measured in voxels using Avizo (Standard and Fire versions, FEI, Hillsboro, United States).

2.2 Downscaling and upscaling method

To ensure the information derived from each image is representative at larger scales, two procedures were performed in this study: downscale sampling from macroscale to sub-nanoscale and upscale calculation from sub-nanoscale to macroscale.

2.2.1 Representative analysis of downscale sampling

To ensure the parameters used for the upscaling procedure were appropriate and accurate, each sub-sample at lower scale (higher resolution) should be representative for the upper scale (lower resolution). Representative analysis was performed at each imaging scale to examine quantitatively whether data extracted from the images was representative at each scale. It consists of two steps: 1) variance analysis of the homogeneous volumes for sub-sample selection at upper scale (see more details in supplementary online materials); 2) representative volume analysis for the features in the selected sub-samples at lower scale (see Ma et al., 2016).

2.2.2 Three- stage upscaling procedure

The principle for upscaling used in this study is to use lower scale (small samples with high resolution) information to derive governing equations for microstructure and pore information which are also valid at an upper scale (large sample with low resolution).

The three-stage upscaling procedure bridges adjacent scales using volume coefficients at three stages to link the large range of scales. A volume coefficient is defined as the volume ratio of a specific feature to its dependent feature (see Figure 2). For example, the volume coefficient for pore type I (intra-organic pores; Φ_1) at the nano-scale is calculated from the ratio of the volume of porosity inside organic matter (a typical feature at nanoscale) to the total volume of organic matter (a typical feature at sub-micron scale). The parameters used to derive the upscaling equations at the four different length scales encompass five major compositional 'phases': fractures (macroscale), laminae (microscale), mineral grains and organic matter (sub-micron scale), and pores (nanoscale to sub-nanoscale). Further, our multi-stage upscaling

method utilizes the corresponding phases (pore, mineral, lamina and fractures) at multiple length scales, as illustrated both schematically and using a real shale sample in Figure 2. The 2D sketch shows the downscaling sub-sample selection and the 3D images (perspective projections) show the corresponding 3D images collected and the key features identified (*XZ* directions show the bedding planes in macroscale to sub-micron scale, and *XY* directions show the bedding while *Z* shows the milling planes in nanoscale and sub-nanoscale. Equations were derived and the parameters quantified for these typical samples, and were extended to samples at different depths in the core, using lab-measured TOC and XRD (Table 4).

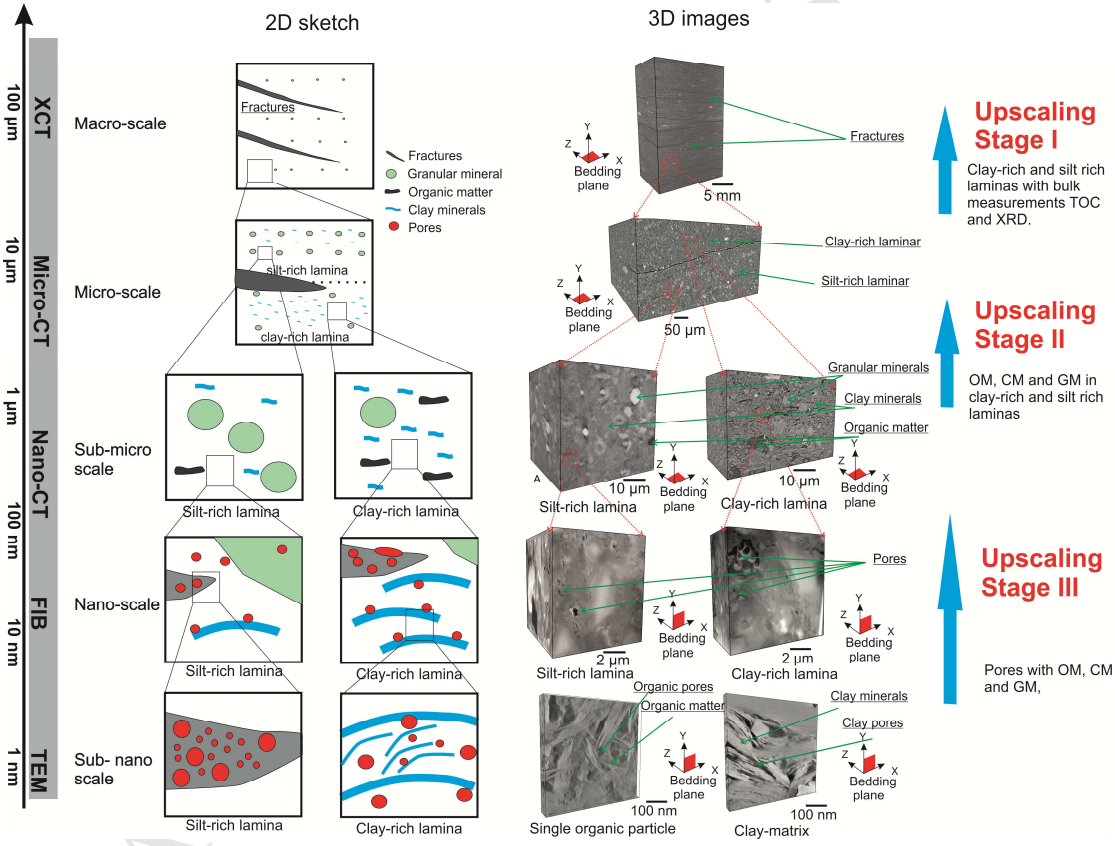

Figure 2 Schematic sub-sample selection and three-stage upscaling method for porosity from sub-nanoscale to macroscale. The axis on the left shows the scales and the imaging techniques used. The rightmost column shows the three-stage upscaling method used in this study.

3 Results

3.1 Petrological and petrophysical characteristics

The selected Haynesville-Bossier Shale sample is dark grey in color and fissile in texture. Thin section observations under the optical microscope show that the sample contains mineralogically-defined laminae and both continuous and disrupted fractures parallel to the bedding plane (Figure 3 AI). Silt-rich laminae are 1-3 mm thick and contain large volumes of silt-sized grains including carbonate peloids, quartz and feldspar. The phyllosilicate-rich laminae are also 1-3 mm thick, but consist of lenticular phyllosilicate mineral-rich peloids and irregular and elongated organic matter pieces. SEM observations (Figure 3 AII- AIV) of polished thin sections revealed that detrital quartz and calcite are major silt components, ferroan dolomite, non-ferroan dolomite, chlorite, albite and quartz cements were also observed. The matrix is composed of scattered organic matter grains and phyllosilicate minerals including muscovite and chlorite. TOC-corrected XRD and energy-dispersive X-ray spectroscopy (EDX) data show that mineral components of the sample include granular quartz, calcite, dolomite, albite and pyrite and phyllosilicate minerals including chlorite (chamosite) and muscovite (Table 1). The proportions of phyllosilicate minerals, granular minerals and organic matter are 53, 39 and 8 vol% respectively. Additionally, the helium porosity for this sample is 7.0 % ±0.1%.

Table 1 Mineralogical results from XRD measurements

Minerals	XRD and TOC (wt %)	Component assemblage	XRD and TOC derived weight percent (wt %)	Imaging derived volume percent (vol %)
Quartz	25±1%	Granular minerals	55 ±5%	53 ±5%
Calcite	14±1%			
dolomite	6±1%			
Albite	9 ±1%			
Pyrite	1 ±1%			

chlorite	18 ±1%	Phyllosilicate minerals	41±2%	39 ±2%
Muscovite	23 ±1%			
TOC	4±1%	Organic matter	4±1%	8±1%

3.2 Microstructure quantification

Five 'phases' were identified and quantified over the range of scales and resolutions: fractures, siliceous silt, organic matter, phyllosilicate minerals and pores (Figure 3). Images at macroscale to sub-micron scale shown in Figure 3 are XCT images and images at nanoscale are FIB images. Images at sub-nanoscale are ET images.

At the lowest resolution (macroscale, 13.3 µm/voxel size, sample ~15 mm in diameter), textural features are visible; phyllosilicate- and silt-rich laminae can be observed (Figure 2 row I). The silt-rich laminae contain a greater volume of silt-size grains (> 4 µm) while the phyllosilicate-rich laminae contain higher volumes of 'matrix material' (defined at this resolution as phyllosilicate minerals, organic matter and pores). The microfacies classification relies on the silt concentrations in both the silt-rich and phyllosilicate-rich laminae. Fractures and large grains (>40 µm) and are the only features visible in the sample at the hand-specimen scale. Fractures with widths of 40-80 µm were observed parallel to bedding and account for 1.2 vol% of the sample (Figure 3 A1). Large grains are primarily carbonate peloids and comprise 3 % of the total sample volume (Figure 3 BI). The majority of these grains are 40-100 µm in size and have no preferred orientation. Due to the small size of the sample components and the limits of resolution of the technique at this scale, data on components below 13 µm in size are only collected using higher resolution techniques. The quantified error of the volume percentages at this scale is ± 6%.

At the microscale (0.5 µm/voxel, sample ~1 mm in diameter), microfractures and granular minerals were observed (Figure 2 row II). At this scale, the higher resolution enables clear definition of fracture boundaries, and small branching fractures can be identified (Figure 3 AII). Fractures comprise 2 vol % of the total sample, and apertures range from 1 to 32 µm. Granular minerals account for 23 vol % of the total sample (Figure 3 BII), and comprise 96

vol% of silt-size (4- 62.5 µm) and 4 vol % of fine phyllosilicate grains (<4 µm). The quantified error of the volume percentages at this scale is ± 4%.

Two cuboid-shaped volumes (sample ~65 µm in diameter) at the sub-micron scale (0.06 µm /voxel) (Figure 3 row III and IV) were obtained on the silt- and phyllosilicate-rich laminae components. At this resolution, granular minerals including quartz and calcite can be differentiated. Although 'matrix material' (consisting of organic matter, phyllosilicate minerals and pores) can be identified, they are not fully resolvable at this scale. The sub-micron scale-1 data (in silt-rich laminae; Figure 3 row III) is from a silt-rich lamina with similar fractions of granular minerals (45 vol %) and phyllosilicate minerals (50 vol %). Organic matter particles are thin (0.1-2.0 µm) and elongate (30-80 µm long) with a volume of 5 vol %. The sub-micron scale-2 data (in phyllosilicate-rich laminae; Figure 3 row IV) is from a phyllosilicate-rich lamina and consists of isolated granular minerals (18 vol %) and connected phyllosilicate minerals (77 vol %). Organic matter particles are relatively large in size (0.6-4.0 µm) and form a significant volumetric component (5 vol %), but are isolated. Organic matter and phyllosilicate mineral phases at this scale that are associated with pores cannot be segmented due to their small sizes. Therefore, pores are included in the organic matter and phyllosilicate mineral volumes at this scale, at which the quantified error of the volume fractions is ± 3 %.

The imaging and quantification of small pores and other components can only be achieved at the nanoscale (Figure 3 row V and VI; sample ~8 µm in diameter). The voxel size is 0.01µm in the *XY* plane (SEM image slices) and 0.02µm in the *Z* direction (the milling direction). Image sizes at the nanoscale are only a few microns across, which is not large enough to provide representative data on granular minerals. Therefore, two FIB-SEM datasets were collected in order to provide a more representative dataset. The nanoscale-1 data (in a silt-rich lamina; Figure 3 row V) has an organic matter content of 10.7 vol % with laminar organic particles in the 0.02-3.00 µm (equivalent spherical diameter) range and the majority of particles fall into at 0.02-0.06 µm. Large subangular grains of granular minerals in the 0.08-

3.00 µm range occupy a large volume fraction of 46.1 vol %, and small phyllosilicate minerals with equivalent (Feret) diameter 0.02-0.20 µm occupy 38.4 vol%. Corresponding porosity for image nanoscale-1 is 4.8 vol %. The nanoscale-2 volume (in a phyllosilicate-rich lamina; Figure 3 row VI) has a higher organic matter content of 21.2 vol%, a granular mineral content of 41.2 vol% and phyllosilicate mineral content of 33.0 vol%, with similar grain sizes to nanoscale-1. The porosity of image nanoscale-2 is 4.6 vol %. The volume percentage error at this scale is ± 0.5 %.

Pore under 20 nm can be only imaged and quantified at the sub-nanoscale (Figure 3 row VII and VIII). ; The sample sizes are around 600 nm in XY plane and 200nm in the Z direction with 0.6 nm voxel size. Two image sets of pores in single organic particle and in phyllosilicate-matrix were collected respectively. The organic matter particle occupies 37.7 vol% and the pores with in organic matter occupy 4.8%. The phyllosilicate-matrix is quantified to be 87.8 vol% with 13.2 vol% pores in between. The volume percentage error at this scale is ± 0.8 %.

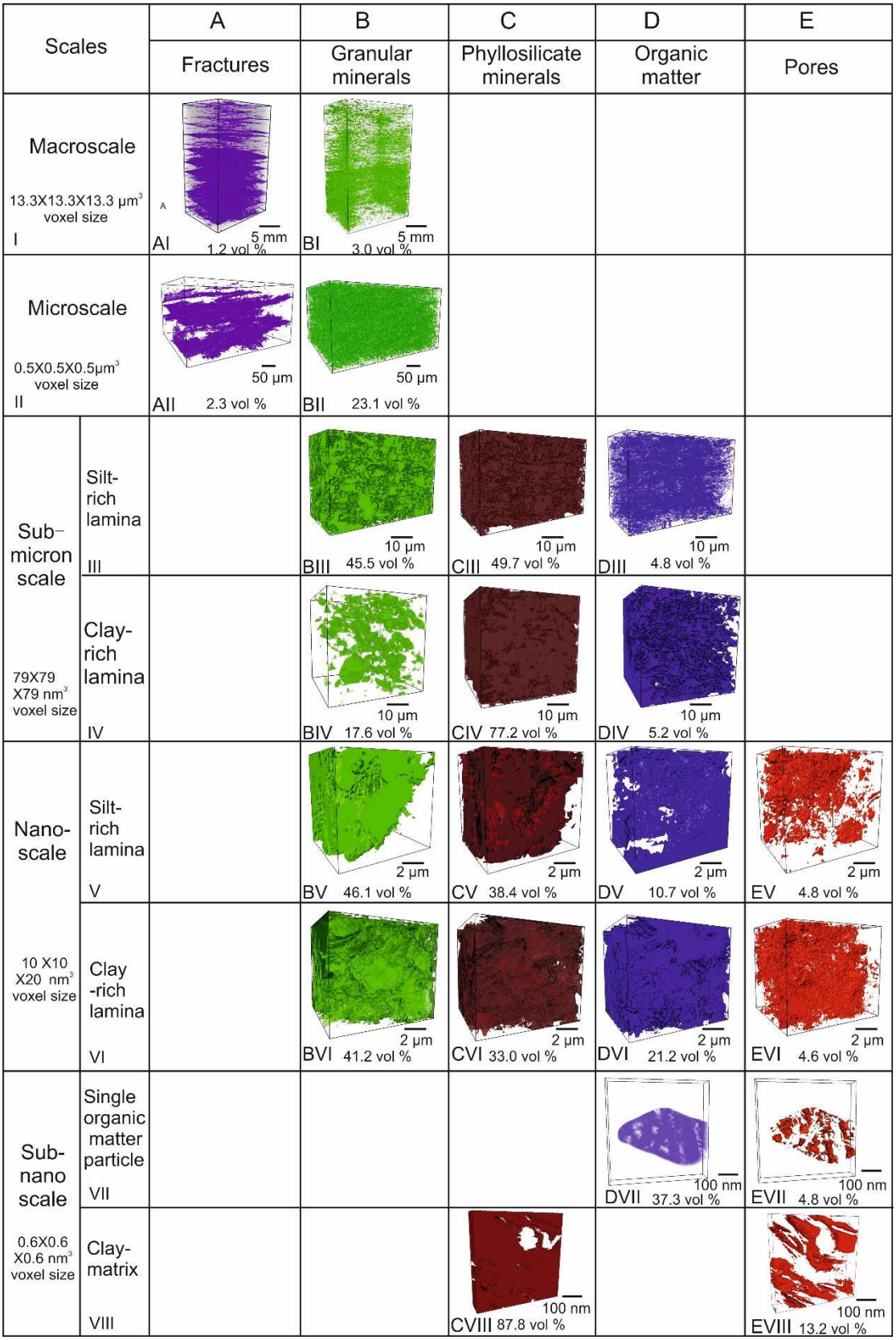

Figure 3 Multi-scale images of fractures, granular minerals, phyllosilicate minerals, organic matter and pores. A: segmented fractures, B: segmented granular minerals, C:

segmented phyllosilicate minerals; D: segmented organic matter; E: segmented pores.

(Colors refer to different segmented phases.)

3.3 Pore system quantification

The pore system consists of fractures and pores. Fractures were quantified at macroscale and microscale while the pore systems were quantified at the nanoscale and sub-nanoscale owing to the field of views and voxel sizes of the images. Specifically, pores were categorised into four types at nanoscale, and two types can be recognized at sub-nanoscale (Ma et al., 2018).

3.3.1 Fractures at macroscale and microscale

Fractures are defined as voids with length/width ratios larger than 10, which are visible at the microscale and above (Figure 3 BI and BII). The width of microscale fractures ranges from 1.5 - 80 µm, and the majority of them are subparallel to the bedding plane.

3.3.2 Pores at nanoscale

(1) Intra-organic pores (type I)

Intra-organic pores are completely bounded by organic matter, usually have spherical or ellipsoidal geometries (Figure 4 A, E and I) and typically range in size from 20-100 nm (Figure 5 A and E). In both the nanoscale-1 and nanoscale-2 datasets the distribution of pore equivalent diameters is similar with a major peak at 0.03-0.04 µm and a minor peak at 0.2 µm (Figure 5 A and E). Pore volume distributions differ in each nanoscale dataset, but both have bimodal distributions with peaks ranging between 0.2 - 0.6 µm (nanoscale-1) and 0.3 - 1.0 µm (nanoscale-2). The nanoscale-1 dataset has a surface area peak range of 0.1 - 0.7 µm and the nanoscale-2 data has a peak range of between 0.2 - 1.0 µm (Figure 5 A and E).

(2) Organic-mineral interface pores (type II)

Organic-mineral interface pores occur at the interface of organic matter and other minerals, particularly between organic matter and phyllosilicate minerals (Figure 4 B). The pores have irregular boundaries, with crack-like or elongate morphologies (Figure 4 B, F and J). The

equivalent diameter distributions of type II pores in two datasets are similar, with major peaks at 0.05-0.06 µm and minor peaks at 0.20 µm. The volumes and surface areas peak at around 1 µm (Figure 5 B and F) in both datasets.

(3) Inter-mineral pores (type III)

Inter-mineral pore geometries are elongated, lenticular or spherical and occur between individual phyllosilicate mineral grains and other mineral phases (Figure 4 C, G and K). Where type III pores occur between phyllosilicate minerals, especially muscovite and chlorite, they have wedge-like elongated morphologies. Type III pores associated with granular mineral grains have lenticular and irregular morphologies (Figure 4 C). Pore equivalent diameters in the nanoscale-1 volume have a major peak at 0.03-0.04 µm and a minor peak at 0.20 µm. The pore equivalent diameter distribute in the nanoscale-2 volume has a major peak at 0.04-0.05 µm with a minor peak at 0.20 µm (Figure 5 C and G). Volume and surface area distributions in the nanoscale-1 volume both peak at 0.20 µm; while in the nanoscale-2 volume type III pores have bimodal volume and surface area distributions with peaks at 0.2 and 2.0 µm respectively (Figure 5 C and G).

(4) Intra-mineral pores (type IV)

Intra-mineral pores are present within quartz, calcite, albite, ankerite and pyrite framboid mineral grains (Figure 4 D). Type IV pores have polygonal or irregular spherical morphologies, particularly where they occur within carbonate grains and pyrite framboids (Figure 4 D, H and L). Compared with the other three pore types, pore type IV has the smallest diameter which is in the range of 0.02-0.20 µm, with a peak at 0.03 µm. The volume and surface area distributions peak at 0.06 µm in the nanoscale-1 and 0.20 µm in nanoscale-2 volumes (Figure 5 D and H).

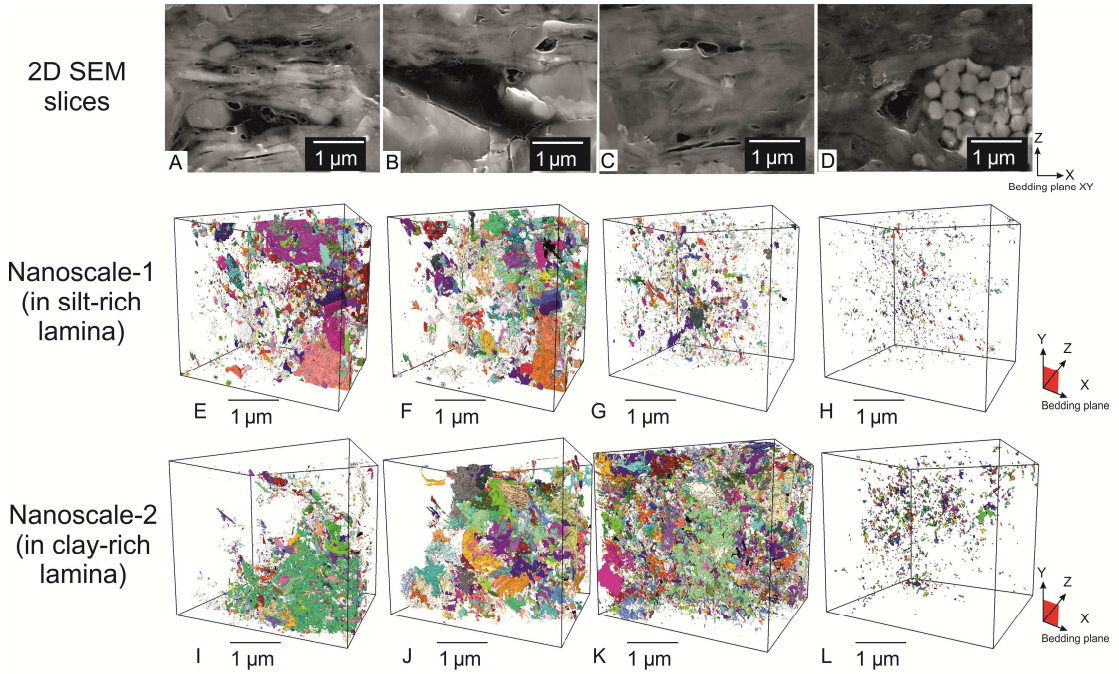

Figure 4 Sub-micron scale pore systems. A-D SEM images of intra-organic, organic mineral interface, inter- and intra-mineral pores. E-H 3D renderings (perspective projections) of the four pore types in nanoscale-1 (silt-rich lamina), I-J in nanoscale-2 (phyllosilicate-rich lamina). Here the *XY* plane is parallel to bedding.

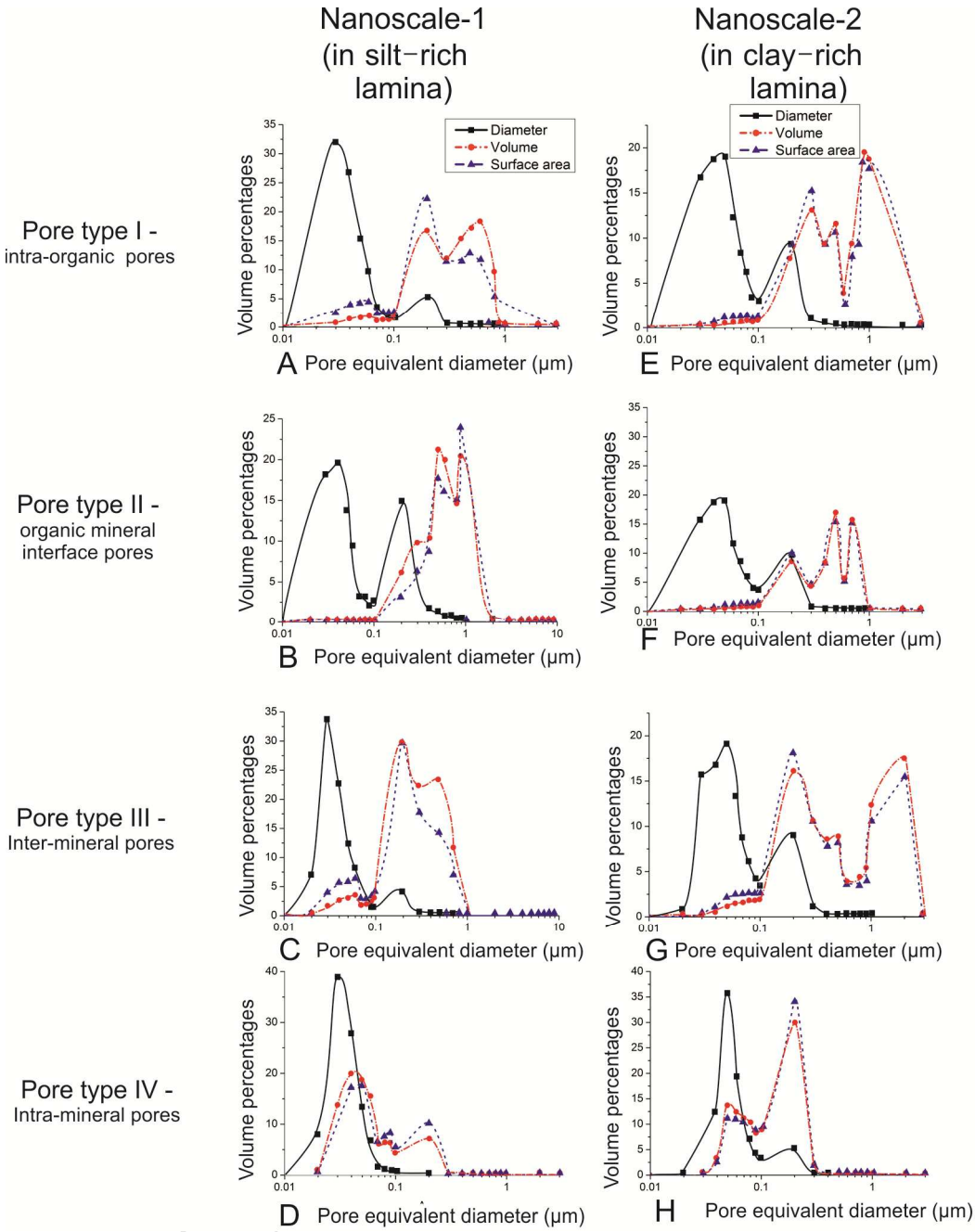

Figure 5 Equivalent diameter, volume, and surface area distribution of the four pore types in nanoscale-1 (in silt-rich lamina) and nanoscale-2 (in phyllosilicate-rich lamina) data sets, and the corresponding average pore equivalent diameter of four pore types.

3.3.3 Pores at sub-nanoscale

Pores below 20 nm can only be directly imaged only using the ET technique. They include intra-organic pores and inter-mineral pores (Figure 6 A-D). These images do not provide representative information due to the small sample sizes (600nm ×600 nm ×60 nm), but they provide the typical parameters of nanopores within carefully selected sample volumes. Pores below 20 nm occupy 4% of pores 1-100 nm for IntraO pores and 7% for InterM pores based on the TEM image analysis (Figure 6 E-F). Despite their small size and representing a small fraction of the total pore volume, our previous work (Ma et al. 2018) has shown that pores at 10 - 100nm can be well connected, strongly oriented parallel to bedding, dominate gas flow in shales and account for their low permeabilities and permeability anisotropy. Pores smaller than 10 nm are comparable to interatomic dimensions and the flow can be diffusive or transition flow (Javadpour et al., 2007).

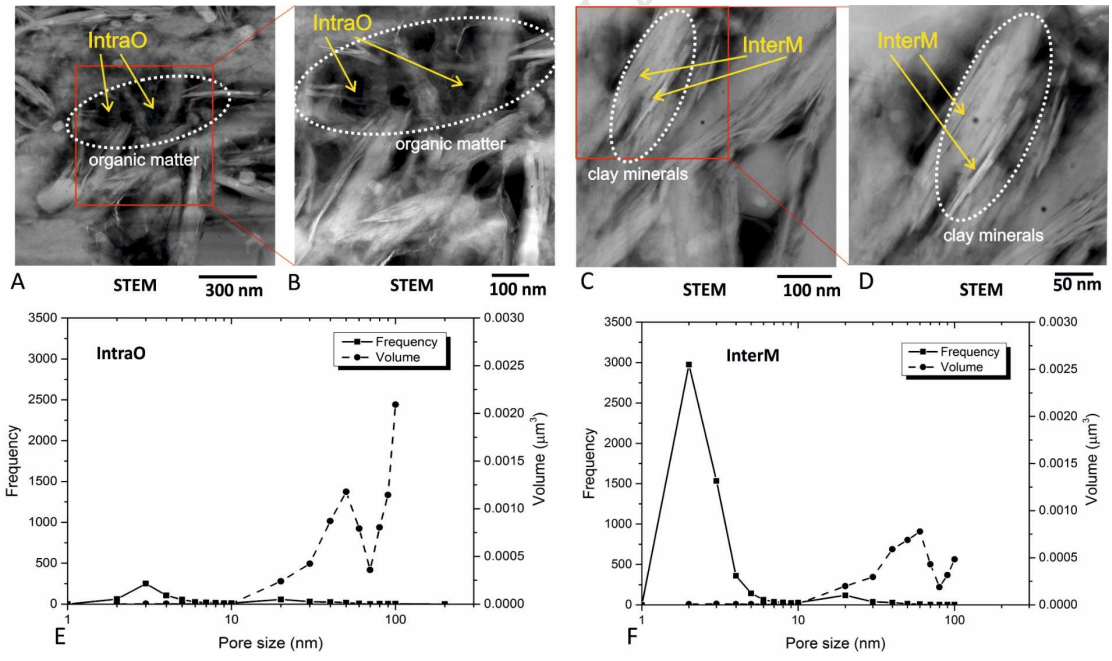

Figure 6 Pores observed in the TEM images and their size distributions. A-B: images of intra-organic pores; C-D: images of inter-mineral pores; E: pore size distribution of intra-organic pores; F: pore size distribution of inter-mineral pores

Pores below 20 nm can also be detected using BJH pore size distribution derived from nitrogen sorption techniques (Figure 7). The pore size distributions are displayed on the basis of BJH theory and are shown with major peaks around 2 nm and minor peaks at 50-60 nm (Figure 7 B). Based on hysteresis loops and following de Boer's identification (De Boer and Lippens, 1964), pore shapes are interpreted to be wedge-shaped (Figure 7 A), or to have a very small aspect ratio (i.e. thin relative to length), which corresponds with the STEM observation in this study.

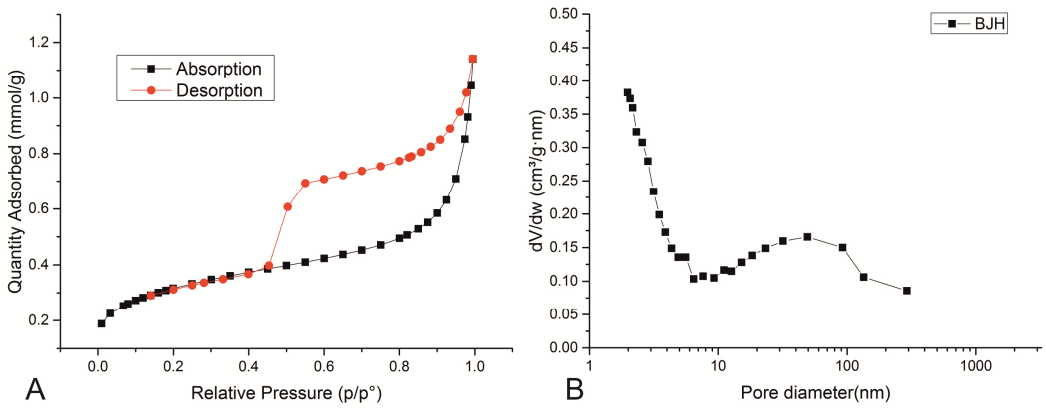

Figure 7. Nitrogen sorption measurements (A) and BJH pore size distribution (B)

3.4 Downscaling and upscaling quantification

3.4.1 Representative analysis

The two-step representative analysis (variance analysis and representative volume analysis verifies that the quantitative data at each scale is characteristic of the sample at that scale. Pores can only be discriminated at the nanoscale and sub-nanoscale according to image resolution limitations (see more details in result 3.2 and 3.2). Images at sub-nanoscale resolutions are not representative and therefore are not shown in Figure 8. The minimum representative pore volumes and their dependent phases (i.e. intra-organic pores and their host organic matter particles) are 5 μm edge-length cubes. Organic matter, phyllosilicate minerals and granular minerals can be distinguished at the sub-micron scale within dependent silt-rich and phyllosilicate-rich laminae (microfacies). The minimum representative volumes for this

scale are 13 and 20 μm (per side of cube) for sub-micron scale-1 (in silt-rich laminae) and sub-micron scale-2 (in phyllosilicate-rich laminae), respectively. At the microscale, granular minerals and fractures have a minimum representative volume value of 320 μm. At the macroscale, this value increases to 7 mm edge-length cube. REV is only considered for the unfractured sample volume at microscale and with artificial fractures at macroscale. The whole sample representative elementary volume (REV) can be calculated when independent phase associations (i.e. microfacies) are detected, as the other features (e.g. minerals, organic matter and pores) are dependent upon these phase associations. Therefore, REV for unfractured volume in this sample is 320 μm. It increases to 7 mm when large artificial fractures are removed from consideration.

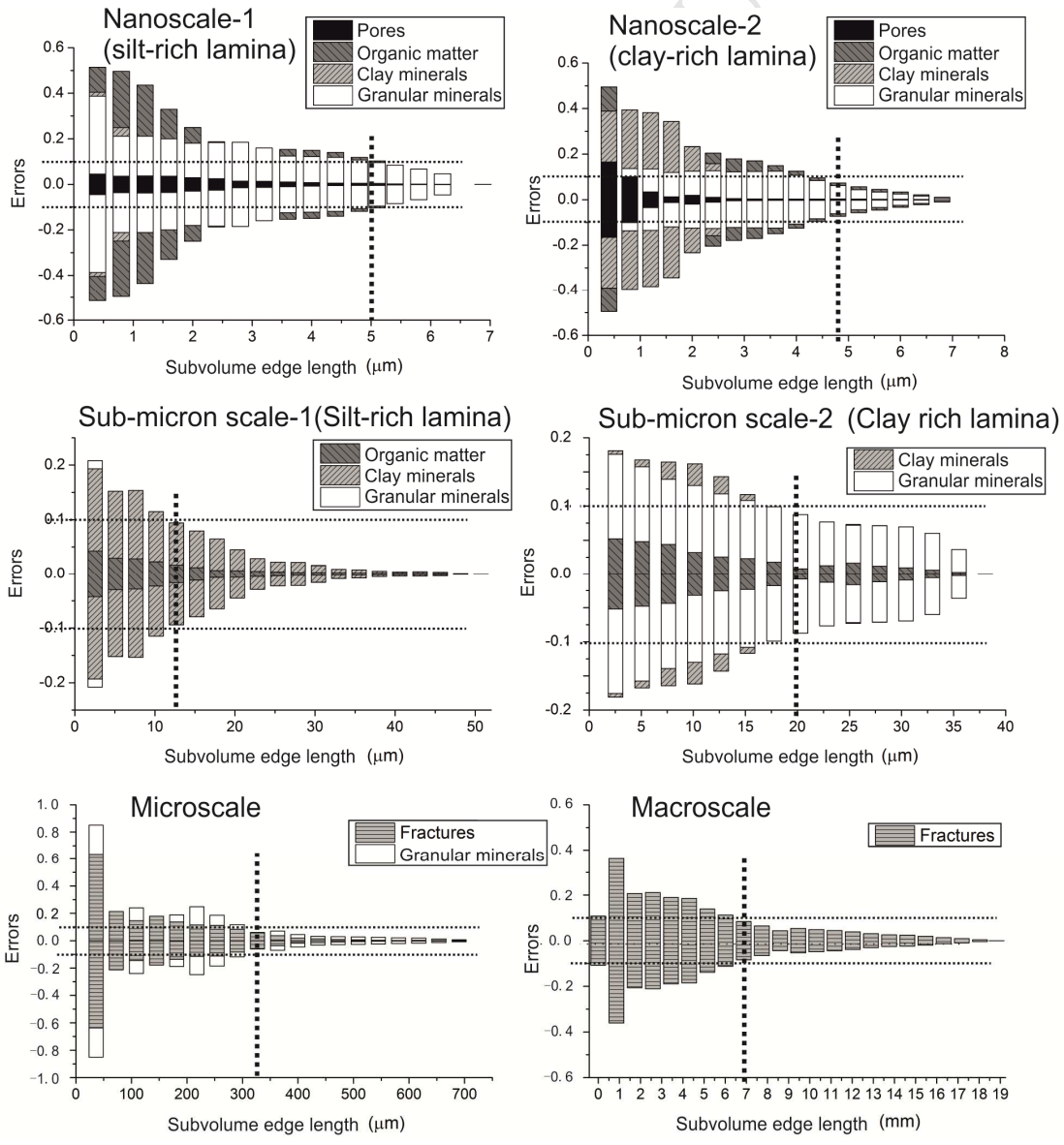

Figure 8 Representative volume analysis from nanoscale to macroscale. Volume fractions of single or combined phases are selected from granular minerals, phyllosilicate minerals, organic matter and pores shown, vertical dash lines show the minimum representative volume for each data set.

3.4.2 Equation deduction

Heterogeneity presents a challenge in understanding shale pore systems. Imaging and quantification datasets suggest pores are closely related to organic matter, phyllosilicate minerals and granular minerals at sub-nanoscale to nanoscale. At the microscale, organic matter, phyllosilicate mineral and granular mineral contents are related to silt-rich and phyllosilicate-rich laminae. These laminae together with fractures represent the whole sample at the macroscale. Therefore, a three-stage upscaling method was developed, encompassing (i) pore to mineral and organic matter, (ii) mineral to laminae, and (iii) laminae to bulk measurement.

Upscaling stage I:

Total macroscale porosity at final upscaling step:

$$V_p = V_f + V_{p1} + V_{p2} + V_{p3} + V_{p4} \quad (1)$$

$$= V_f + \Phi_1 \times V_{OM} + \Phi_2 \times V_{OM} + \Phi_3 \times V_{CM} + \Phi_4 \times V_{GM} \quad (2)$$

where V_p is the total porosity (%), V_f is the volume percentage of fractures, V_{p1} to V_{p4} are the volume percentage of four pore types, Φ_I to Φ_4; refer to the volume coefficients of four pore types and corresponding phases (OM- organic matter, CM- phyllosilicate minerals, GM- granular minerals),

Upscaling stage II:

Φ_i (i = 1-4) can be calculated at the this step

$$\Phi_i = \Phi_{i\text{-}sl} \times V_{sl} + \Phi_{i\text{-}pl} \times V_{pl} \quad (3)$$

$\Phi_{i\text{-}sl}$ and $\Phi_{i\text{-}cl}$ refer to the volume coefficients of the four pore types in silt-rich

laminae and phyllosilicate-rich laminae. V_{sl} and V_{pl} are the volume percentages of silt-rich laminae and phyllosilicate-rich laminae.

Upscaling stage III:

$\Phi_{i\text{-}sl\ and}\ \Phi_{i\text{-}pl}$ can be only calculated at nano-scale and sub-nanoscale, from the volume ratios of the four pore types and the corresponding phases (organic matter, granular minerals and phyllosilicate minerals) in two laminae, respectively.

3.4.3 Upscaling calculation

The volume coefficients in silt-rich laminae ($\Phi_{i\text{-}sl}$) and phyllosilicate-rich ($\Phi_{i\text{-}pl}$) laminae were calculated based on the images at sub-nanoscale and nanoscale (Table 2). The quantification of the laminae themselves occurs at the microscale, and they can be regarded as a microfacies in unlaminated samples. The percentages of silt-rich laminae and phyllosilicate-rich laminae were quantified to be 21 vol.% and 79 vol.% in this sample, therefore the average $\Phi_1\ and\ \Phi_2$ were calculated to be 0.111 and 0.025 (Table 2).

Table 2 volume coefficients (Φ_1, Φ_2, Φ_3, and Φ_4) in upscaling stages one and two

Volume coefficient	Corresponding pore types	Corresponding pore-associated phases	In phyllosilicate rich lamina ($\Phi_{i\text{-}cl}$) *	In silt rich lamina ($\Phi_{i\text{-}cl}$)*	Upscaled (Φ_i)
Φ_1	IntraO	Porous organic matter	0.128 ± 0.05	0.049± 0.05	0.111
Φ_2	InterO	Non-porous organic matter	0.021 ± 0.01	0.039± 0.01	0.025
Φ_3	InterM	Granular minerals	0.087± 0.002	0.083± 0.002	0.086
Φ_4	IntraM	Phyllosilicate minerals	0.002± 0.001	0.002± 0.001	0.002

*uncertainties are given based on one standard deviation

Owing to the low resolution of the imaging technique at the macroscale, only large scale features such as fractures can be distinguished. Porosities were computed based on the

volume fractions of organic matter, phyllosilicate minerals and granular minerals that were calculated from bulk property measurements such as TOC and XRD, and also from the volume coefficients derived above. The volume percentages of kerogen are roughly two times the TOC weight percentages (Ward, 2010).

The total porosity from equation (1) can be estimated using the parameters shown below:

$$\text{Total porosity (\%)} = V_f + \Phi_1 \times V_{OM} + \Phi_2 \times V_{OM} + \Phi_3 \times V_{OM} + \Phi_4 \times V_{OM}$$

$$= 2.4 + 0.111 \times 2 \times \text{TOC} + 0.025 \times 2 \times \text{TOC} + 0.086 \times \text{phyllosilicate mineral content} + 0.002 \times \text{granular mineral content.} \quad (6)$$

The upscaled porosity for the whole sample volume (3375 mm^3) is 7.2%. This is 0.2% higher than the 7.0% measured in an adjacent sample using the helium porosity techniques (Figure 9 A). The curve of cumulative porosity against pore sizes acquired from images corresponds well with that of BJH pore sizes acquired by nitrogen sorption (Figure 9A). The majority of pores larger than 3 µm are represented by fractures, which contribute 2.3 % of total rock volume, and 31.9% of the total porosity. Four peaks are found in the incremental porosity: 30 µm for fractures, 3 µm, 400 nm and 60 nm for pores (Figure 9A). Pores between 20 nm to 3 µm contribute around 4.6 % of the rock volume (63.8 % of the porosity). Pores below 20 nm contribute less than 0.35 % of the rock volume (5% of the porosity). The pore size distributions are shown by pore number density in Figure 8 B to give consistent units for the different volumes of images at each scale. The overlapping data from each image shows similar trends (Figure 9B). Smaller pore sizes contribute more significantly in number density but less in volume.

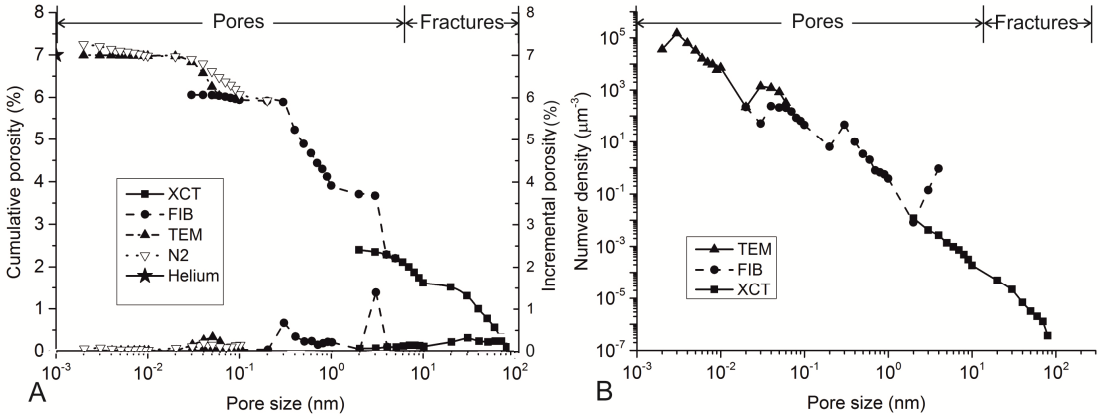

Figure 9 Upscaled pore sizes from 1 nm to 300 μm (A) cumulative pore volume and incremental porosity, and (B) pore number density

The parameters calculated for this sample can be applied to other adjacent samples collected in the same core with similar microstructure. The organic matter content and mineral content were acquired via the TOC and XRD measurements (Table 4). The agreement of calculated porosity (7.2%) at the macroscale is excellently compared to helium porosity (-6.08 % to 8.50 %, see Table 4).

Table 4 Comparison of upscaled porosity with helium porosity, XRD and TOC measurements on core samples taken from the same core at the depths indicated. Uncertainties are given at one standard deviation.

Depth (feet)	Laboratory measurements				Computed values	
	TOC (wt %)	XRD (wt %)		Helium porosity (%)	Calculated Porosity (%)	Difference relative to helium porosity (%)
		Phyllosilicate mineral	Non-phyllosilicate mineral			
11349	1.5 ± 0.1	46 ± 1	54 ± 1	6.8 ± 0.1	6.92	1.81
11402	0.9 ± 0.1	58 ± 1	42 ± 1	7.8 ± 0.1	7.75	-0.16
11442	1.4 ± 0.1	44 ± 1	56 ± 1	6.6 ± 0.1	6.72	1.27
11482	1.3 ± 0.1	45 ± 1	55 ± 1	7.0 ± 0.1	6.78	-2.62
11581	1.9 ± 0.1	48 ± 1	52 ± 1	7.7 ± 0.1	7.21	-6.08
11611	2.1 ± 0.1	41 ± 1	59 ± 1	6.4 ± 0.1	6.69	4.48
11662	2.2 ± 0.1	53 ± 1	47 ± 1	7.1 ± 0.1	7.72	8.50
11692	2.0 ± 0.1	49 ± 1	51 ± 1	7.3 ± 0.1	7.33	0.66
11752	2.4 ± 0.1	42 ± 1	58 ± 1	6.9 ± 0.1	6.86	-0.26

4 Discussion

On account of the heterogeneity of shales, microstructure and pore-fracture system characterisation across scales is not straightforward (Fathi and Akkutlu, 2009; Ross and Bustin, 2009). Therefore, it is important to develop a multi-scale imaging technique and a reliable upscaling approach over a large range of scales. Below, we discuss the deviations between different measurements, the accuracy of the proposed approach, and implications for energy and environmental applications.

4.1 Deviations between parameters from image analysis and bulk measurements

The average difference in the calculated porosity relative to the measured bulk porosity is less than 10% of the measured bulk porosity for the sample tested (Table 4). This discrepancy would suggest that although the method is broadly accurate, some undefined factor(s) might be skewing either the upscaled calculated porosity or the measured bulk porosity. However, this difference is relatively small for such a highly heterogeneous material, and could result from selective sample bias, statistical errors, systemic errors, or one of the factors explored below.

(1) *Different techniques may measure different types and different sizes of porosity*.

The imaging techniques measure pores (whether connected or not) larger than 2 nm, which contribute 7.2% porosity. Nitrogen sorption measures locally connected pores between 2 nm to 300 nm (Seaton and Walton, 1989). Helium porosimetry measures pores above 0.2 nm and larger provided they are connected to the sample surface (Lowell et al., 2012). The measured helium porosity is 7.0%, only 0.2% different from the porosity measured using the imaging technique (Figure 8A). The different sizes and types of pores measured by different techniques, and the physical differences between these techniques can be expected to lead to large deviations. However, our upscaling technique is within the measurement errors. Despite this the difference is small and implies a high degree of connectivity in the imaged pores.

(2) Differences in sample volume, composition and texture. The different techniques measure different sample volumes. These may contain different porosity fractions due to the effect of increasing sample heterogeneity with decreasing sample size. Helium porosity, for example, was measured on a 20 mm diameter shale cylinder (~24g or more), while XRD and TOC measurements require a relatively small weight of powder (1-2 g). Multi-scale images were acquired from samples with dimensions ranging from millimeters to microns. Further, variations in texture and composition between different sample volumes may also impact on measured porosity.

4.2 Are the results truly representative of the quantified microstructure and pore system?

To increase the degree of representativeness of images at lower scale (higher magnifications, higher resolutions), the areas chosen to be typical of a phase were selected from relatively homogeneous volumes at the upper scale (lower magnification images). The selection avoided large features which could be segmented in the upper scale and therefore increase the extent to which images are representative of small features at lower scale. Analysis of variance of the homogeneous volumes for sub-sample selection at the upper scale and representative volume analysis for selected sub-samples at lower scales were both calculated to produce an integrated analysis that was representative overall. In upper scale images, as voxel size decreases and approaches the sample volume of the lower scale image, the variance of each averaged voxel (avoiding the typical features at upper scale) is close to zero. Because variances are close to zero, each averaged voxel is considered to be homogeneous and a random sub-sample was then selected from these volumes. The representativeness analysis is less reliable when the scale of images decreases due to the high heterogeneity and small sample sizes. Moreover, the images at lower scale are normally 1/10 edge length of the upper scale, which corresponds to 1/1000 of the volume.

When investigating samples over four orders of magnitude in length scale, the optimal approach used in imaging studies is to use one or two representative subsamples at each scale.

The representative size for the sub-sample selection and the image itself have both been evaluated in this study. More images at each scale would increase the precision of the volume coefficient calculations and systematic analysis (Kelly et al., 2016), but would be impractical given the scale of the features observed and hence resource requirement. The REV dimension estimated in this study for an unfractured sample volume is 320 μm, which is comparable to representative elementary area (REA) in prior 2D studies. These would be, for example, 200 μm in Haynesville shale (Klaver et al., 2015), 200 μm in Toarcian shale (Houben et al., 2016) and 300 μm in Eagle Ford shale (Adeleye and Akanji, 2017). REV is slightly larger than REA in the same Haynesville-Bossier Shale Formation (Klaver et al., 2015). This may be due to the additional dimension (3D) of the data in this study when compared to the 2D analysis reported elsewhere. The large fractures seen at macroscale are inferred to be artifacts introduced during sample recovery, and REV increases to 7 mm when these artificial fractures are absent.

4.3 Implications for energy and environmental applications

The proposed methods of characterization and representative analysis allow the study of microstructure and pore systems in shales to be extended to a large range of scales. This broad approach provides the opportunity to evaluate economically and environmentally significant applications.

Four types of pores are identified and quantified in this study. The different pore types play different roles for the gas storage and flow in the reservoirs. Intra-organic matter pores can contain a large amount of free and adsorbed gas in shale gas reservoirs (Ambrose et al., 2012), and depleted reservoirs may provide significant pore volumes for carbon dioxide storage. The volume of these pores together with other relevant pore types (i.e. organic-mineral interface pores and inter-mineral pores) can be used to assess the volume of free and adsorbed hydrocarbon gas that may be present or supercritical CO_2 that might be stored. The surface area of intra-organic pores can be used for adsorbed gas calculation as they account for the majority of adsorbed gas (Balashov et al., 2015). Based on pore size quantification, fluid and gas in this sample could be produced via by a combination of flow mechanisms, as

found in other materials with multiple scales of porosity (Tariq et al., 2011). Flow mechanisms may include Knudsen flow in the finest pores, transitioning to Darcy flow or slip flow in the larger pores, according the magnitude of gas pressure. Connected pore networks can be found globally in inter-mineral pores at the nanometer scale and be locally connected to the intra-organic pores (Ma et al., 2018) in shales. These results provide more precise details of the pore structure that can form a basis for modelling.

In the same way, multi-scale characterization of the pore system can be applied for the evaluation of effective cap rocks for carbon and nuclear waste sequestration evaluation immediately (Wollenweber et al., 2010). The larger sized, locally connected pores (for example, intra-organic pores and organic-mineral interface pores) determine the total mass of CO_2 that can be stored within the target shale rocks at a given gas pressure, or escape from underlying formations. The smaller sizes of pores scattered in the sample, such as inter-mineral pores, control the sequestrating capability (capacity and rate) of CO_2 in the target reservoirs.

The characterized microstructures across scales, the relationships between the microstructures and corresponding pores, and the interface of each individual pore can be analyzed directly to provide opportunities to understand the chemical (e.g. Liu et al., 2012) and physical interactions (e.g.Balashov et al., 2015) that are crucial for long-term geological sequestration. Moreover, the proposed multiscale characterization and upscaling methods may have a wider applications in many other materials with complex and heteroporous structures, for example, geothermal reservoirs (Lichtner and Karra, 2014) and fuel cells (Lu et al., 2017).

5 Conclusions

(1) This study presents a multi-stage upscaling method relying on image quantification of textural features from the nanometer to millimeter-scale to quantify pore systems and microstructure in shales. It is the first study to upscale a pore system across four orders of magnitude utilizing 3D images at five distinct resolutions.

(2) A novel two-step analysis, including variance analysis and representative analysis, was proposed and performed to ensure the quantified features in all images are representative at corresponding scales. Meanwhile, it measures the representative elementary volume (REV) of the whole sample. The minimum REV in unfractured volumes in the sample is (320 μm^3) and it increases to (7 mm^3) when artificially fractures are removed from consideration.

(3) The upscaling equations were derived to bridge the four distinct scales through volume coefficient computing at three steps: from pores at nanoscale to porous phase at sub-micron scale, to laminae at microscale and then bulk mineral and organic matter measurement at macroscale. This enables more accurate calculations than in previous studies and results in the computed porosity lying within 7.2 % of the helium porosity.

(4) The upscaled pore system further provides detailed quantification of pore size distributions, pore types and connectivity, which could not be extracted in other studies. The result suggests that the majority of pores larger than 4 µm are represented by fractures, which contribute 2.3 % of total rock volume. Pores between 20 nm to 3 µm contribute around 4.6 % of the rock volume. Pores below 20 nm contribute less than 0.35 % of the rock volume. Also, intra-organic pores have largest volume coefficient and largest sizes, followed by organic-mineral interface pores. Inter-mineral pores contribute most in frequency and connectivity. Intra-mineral pores are relatively small and not connected to the global pore system.

(5) The novel characterization and upscaling method in this study allows the nanoscale microstructure and pore systems to be quantified up to the millimeter-scale, and provide 3D imaged-based information across five scales. The results not only improve the understanding of microstructure and pore system of shales significantly but also permit more accurate assessment for many energy and environmental applications.

6 Acknowledgements

This project was funded in part by the UK-NERC [NE/M001458/1 and NE/R013527/1], the European Union's Horizon 2020 716 Research and Innovation Program under the

ShaleXenvironmenT project, [grant no. 640979] and an industry consortium constituted by Shell (formerly BG Group), Chevron, and Schlumberger. The synchrotron imaging was performed at the Diamond-Manchester Branchline of Diamond Light Source (DLS), Beamtime MT4022. Facilities at the Research Complex at Harwell are gratefully acknowledged, supported in part by the UK-EPSRC [EP/I02249X/1]. BG International (now Shell) provided the Shale sample used in this study.

7 Data Statement:

In accordance with Data Accessibility policy for UK Research Council grant-supported research, the datasets used to generate the graphical presentations in this paper are publically available from the UK National Geoscience Data Centre (NGDC), identified via the above grant numbers. Supplementary Information file with this paper provides the details of the data analysis workflow.

8 References

Adeleye, J.O., Akanji, L.T., 2017. Pore-scale analyses of heterogeneity and representative elementary volume for unconventional shale rocks using statistical tools. Journal of Petroleum Exploration and Production Technology.

Ambrose, R.J., Hartman, R.C., Diaz Campos, M., Akkutlu, I.Y., Sondergeld, C., 2012. New Pore-scale Considerations for Shale Gas in Place Calculations, SPE Unconventional Gas Conference. Society of Petroleum Engineers.

Aplin, A.C., Macquaker, J.H., 2011. Mudstone diversity: Origin and implications for source, seal, and reservoir properties in petroleum systems. AAPG bulletin 95, 2031-2059.

Balashov, V.N., Guthrie, G.D., Lopano, C.L., Hakala, J.A., Brantley, S.L., 2015. Reaction and diffusion at the reservoir/shale interface during CO2 storage: Impact of geochemical kinetics. Applied Geochemistry 61, 119-131.

Barrett, E.P., Joyner, L.G., Halenda, P.P., 1951. The determination of pore volume and area distributions in porous substances. I. Computations from nitrogen isotherms. Journal of the American Chemical society 73, 373-380.

Brunauer, S., Emmett, P.H., Teller, E., 1938. Adsorption of gases in multimolecular layers. Journal of the American Chemical society 60, 309-319.

Busch, A., Alles, S., Gensterblum, Y., Prinz, D., Dewhurst, D.N., Raven, M.D., Stanjek, H., Krooss, B.M., 2008. Carbon dioxide storage potential of shales. International Journal of Greenhouse Gas Control 2, 297-308.

Chen, C., Hu, D., Westacott, D., Loveless, D., 2013. Nanometer□scale characterization of microscopic pores in shale kerogen by image analysis and pore□scale modeling. Geochemistry, Geophysics, Geosystems 14, 4066-4075.

Curtis, M.E., Ambrose, R.J., Sondergeld, C.H., 2010. Structural Characterization of Gas Shales on the Micro- and Nano-Scales, Canadian Unconventional Resources and International Petroleum Conference. Society of Petroleum Engineers.
De Boer, J., Lippens, B., 1964. Studies on pore systems in catalysts II. The shapes of pores in aluminum oxide systems. Journal of Catalysis 3, 38-43.
Fathi, E., Akkutlu, I.Y., 2009. Matrix heterogeneity effects on gas transport and adsorption in coalbed and shale gas reservoirs. Transport in Porous Media 80, 281-304.
Houben, M., Barnhoorn, A., Wasch, L., Trabucho-Alexandre, J., Peach, C., Drury, M., 2016. Microstructures of early jurassic (toarcian) shales of northern Europe. International Journal of Coal Geology 165, 76-89.
Jarvie, D.M., 2012. Shale resource systems for oil and gas: Part 1—Shale-gas resource systems. AAPG Memoir
Javadpour, F., Fisher, D., Unsworth, M., 2007. Nanoscale Gas Flow in Shale Gas Sediments. J. Can. Pet. Technol. 46, 7.
Joyce, S., Hartley, L., Applegate, D., Hoek, J., Jackson, P., 2014. Multi-scale groundwater flow modeling during temperate climate conditions for the safety assessment of the proposed high-level nuclear waste repository site at Forsmark, Sweden. Hydrogeology Journal 22, 1233-1249.
Kazemi, A., Shaikhina, D.S., Pickup, G.E., Corbett, P.W., 2012. Comparison of Upscaling Methods in a Heterogeneous Carbonate Model, SPE Europec/EAGE Annual Conference. Society of Petroleum Engineers.
Keller, L.M., Schuetz, P., Erni, R., Rossell, M.D., Lucas, F., Gasser, P., Holzer, L., 2013. Characterization of multi-scale microstructural features in Opalinus Clay. Microporous and Mesoporous Materials 170, 83-94.
Kelly, S., El-Sobky, H., Torres-Verdín, C., Balhoff, M.T., 2016. Assessing the utility of FIB-SEM images for shale digital rock physics. Advances in Water Resources 95, 302-316.
Klaver, J., Desbois, G., Littke, R., Urai, J.L., 2015. BIB-SEM characterization of pore space morphology and distribution in postmature to overmature samples from the Haynesville and Bossier Shales. Marine and Petroleum Geology 59, 451-466.
Lichtner, P.C., Karra, S., 2014. Modeling multiscale-multiphase-multicomponent reactive flows in porous media: Application to CO2 sequestration and enhanced geothermal energy using PFLOTRAN. Computational Models for CO2 Geo-sequestration & Compressed Air Energy Storage, 81-136.
Liu, F., Lu, P., Griffith, C., Hedges, S.W., Soong, Y., Hellevang, H., Zhu, C., 2012. CO2–brine–caprock interaction: Reactivity experiments on Eau Claire shale and a review of relevant literature. International Journal of Greenhouse Gas Control 7, 153-167.
Loucks, R.G., Reed, R.M., Ruppel, S.C., Jarvie, D.M., 2009. Morphology, Genesis, and Distribution of Nanometer-Scale Pores in Siliceous Mudstones of the Mississippian Barnett Shale. Journal of Sedimentary Research 79, 848-861.
Lu, X., Taiwo, O.O., Bertei, A., Li, T., Li, K., Brett, D.J.L., Shearing, P.R., 2017. Multi-length scale tomography for the determination and optimization of the effective microstructural properties in novel hierarchical solid oxide fuel cell anodes. Journal of Power Sources 367, 177-186.
Ma, L., Dowey, P., Fauchille, A.-L., Taylor, K., Lee, P., 2017a. Correlative multi-scale 3D imaging of shales: An example from the Haynesville-Bossier Shale, southeast USA, EGU General Assembly Conference Abstracts, p. 3809.
Ma, L., Slater, T., Dowey, P.J., Yue, S., Rutter, E.H., Taylor, K.G., Lee, P.D., 2018. Hierarchical integration of porosity in shales. Scientific Reports 8, 11683.
Ma, L., Taylor, K.G., Dowey, P.J., Courtois, L., Gholinia, A., Lee, P.D., 2017b. Multi-scale 3D characterisation of porosity and organic matter in shales with variable TOC content and thermal maturity: Examples from the Lublin and Baltic Basins, Poland and Lithuania. International Journal of Coal Geology 180, 100-112.
Ma, L., Taylor, K.G., Lee, P.D., Dobson, K.J., Dowey, P.J., Courtois, L., 2016. Novel 3D centimetre-to nano-scale quantification of an organic-rich mudstone: The Carboniferous Bowland Shale, Northern England. Marine and Petroleum Geology 72, 193-205.

McKernan, R., Mecklenburgh, J., Rutter, E., Taylor, K., 2017. Microstructural controls on the pressure-dependent permeability of Whitby mudstone. Geological Society, London, Special Publications 454, SP454. 415.
Milliken, K.L., Rudnicki, M., Awwiller, D.N., Zhang, T., 2013. Organic matter–hosted pore system, Marcellus Formation (Devonian), Pennsylvania. AAPG Bulletin 97, 177-200.
Peng, S., Yang, J., Xiao, X., Loucks, B., Ruppel, S., Zhang, T., 2015. An Integrated Method for Upscaling Pore-Network Characterization and Permeability Estimation: Example from the Mississippian Barnett Shale. Transport in Porous Media, 1-18.
Ross, D., Bustin, R.M., 2009. The importance of shale composition and pore structure upon gas storage potential of shale gas reservoirs. Marine and Petroleum Geology 26, 916-927.
Schieber, J., Zimmerle, W., Sethi, P.S., 1998. Shales and mudstones(Volume I, Basin studies, sedimentology, and paleontology).
Slatt, R.M., O'Brien, N.R., 2011. Pore types in the Barnett and Woodford gas shales: Contribution to understanding gas storage and migration pathways in fine-grained rocks. AAPG Bulletin 95, 2017.
Tariq, F., Lee, P., Haswell, R., McComb, D., 2011. The influence of nanoscale microstructural variations on the pellet scale flow properties of hierarchical porous catalytic structures using multiscale 3D imaging. Chemical Engineering Science 66, 5804-5812.
Wang, F.P., Hammes, U., Li, Q., 2013. Overview of Haynesville Shale properties and production.
Ward, J., 2010. Kerogen Density in the Marcellus Shale, SPE Unconventional Gas Conference. Society of Petroleum Engineers, Pittsburgh, Pennsylvania, USA.
Wollenweber, J., Alles, S., Busch, A., Krooss, B., Stanjek, H., Littke, R., 2010. Experimental investigation of the CO2 sealing efficiency of caprocks. International Journal of Greenhouse Gas Control 4, 231-241.
Zhang, S., Klimentidis, R.E., Barthelemy, P., 2012. Micron to millimeter upscaling of shale rock properties Based on 3D imaging and modeling. Exxomobil Upstream Research Co., Houston, Tx, USA. VSG-Visualisation Sciences Group, Burlinton, MA, USA.